Efficient White Light-Emitting Ag-doped CeO$_2$ Nanoparticles Exhibiting Color Temperature Tunability and High Color Rendering

M. Kiran[1] · N. S. Leel[1] · B. Dalela[2] · Mohd. A. Khan[1] · A. Bhargava[1] · D. Lovevanshi[1] · P. A. Alvi[3] · Shalendra Kumar[4] · S. Dalela[1]

Abstract

The present manuscript reports the synthesis of undoped CeO$_2$ and Ce$_{1-x}$Ag$_x$O$_2$ ($x = 0.03$, 0.05, and 0.07) nanoparticles using a microwave-assisted co-precipitation route to understand the Ag doping effect in CeO$_2$ nanoparticles. The structural and optical properties of these nanoparticles were investigated using x-ray diffraction, UV–Vis–NIR, and PL spectroscopy. The XRD result confirmed the formation of cubic fluorite structures with undoped and Ag-doped CeO$_2$ nanoparticles. The crystallite size of Ag-doped CeO$_2$ nanoparticles was observed within the range of 26–47 nm. The absorption peak was observed using UV–Vis–NIR spectroscopy and obtained at below 400 nm, indicating a blue shift with the incorporation of Ag$^+$ ions in the CeO$_2$ nanolattice, and the causes are explained in terms of the BM effect and electronic transitions. The PL measurements were taken to determine the defects and excitation wavelength. The prepared samples depicted good luminescence properties with a high value color rendering index (CRI). The results demonstrated that Ag-doped CeO$_2$ nanoparticles can be used for white light emission, since the structural and optical properties of semiconductors were enhanced upon doping with elements such as Ag. Therefore, these nanoparticles may act as promising candidates for various applications such as UV-absorption, photocatalysis, light-emitting diodes, luminescence, and optoelectronics.

Keywords Ag-doped CeO$_2$ nanoparticles · absorption spectroscopy · oxygen vacancies and defects · blue shifting · photoluminescence · CRI · white light emission

Introduction

Nanocrystal-based optoelectronic devices have been successful in the area of device research. their emitters have been proven to have wide application, especially in white light sources. Generally, light-emitting diodes (LEDs) are more commonly preferred owing to their good advantages over conventional lamps.[1] Since the light industry, including factories, offices, laboratories, streets, workshops, and public places, require more illumination with white light for performing tasks such as writing, reading, and detection, white LEDs are thus inevitable at such places. The color field of LEDs is characterized as "warm white" (< 3300 K), "neutral white" (3300–5300 K), and "cool light" also known as daylight (> 5300 K), based on the IEC standard. Lamps with a correlated color temperature (CCT) (> 4000 K) or more with the color neutral white are recommended for illumination in professional applications.[2] The main purpose of this manuscript is to lay out the structural, optical, and photoluminescence characteristics of Ag-doped CeO$_2$ nanoparticles. Cerium oxide (ceria or CeO$_2$), a rare-earth oxide semiconductor, which has recently attracted much interest due to its exceptional unique features and possible uses, which include solid oxide fuels and superior electrocatalytic performance.[3] The transition of Ce from a Ce^{4+} ion to a Ce^{3+} ion allows it to be widely used for oxidation reactions

✉ S. Dalela
  sdalela@uok.ac.in

1 Department of Pure and Applied Physics, University of Kota, Kota, Rajasthan 324005, India

2 Department of Physics, Government Khetan Polytechnic College, Jaipur 302017, India

3 Department of Physics, Banasthali Vidyapith, Banasthali, Rajasthan 304022, India

4 Department of Physics, University of Petroleum and Energy Studies, Dehradun 248007, India

and oxygen storage capacity. Ceria also plays an important role in applications in the automobile, electrical, metallurgical, medical, optical, and optoelectronic industries.[4-8] CeO_2 possesses diamagnetic behavior in its bulk form but shows a ferromagnetic nature when reduced to nanoparticles, which is convenient for spintronics.[9] Reducing the particle size of ceria is expected to result in a large number of oxygen vacancies. CeO_2 is an *n*-type semiconductor with a band gap energy equal to nearly 3.2 eV,[10, 11] which allows it to act as a UV blocker and glass polishing material.[12] The incorporation of metal ions into metal oxide semiconductors is responsible for the formation of quasi-stable energy states, causing variations in band gap energy and, therefore, tuning the optical properties.

Numerous investigations on the incorporation of other elements into the CeO_2 structure have been conducted to enhance the properties of the materials and to broaden their use. According to Habib et al.[13] the CeO_2 structure increases its catalytic activity when doped with Cr. Leel et al.[14] reported that Ho-doped CeO_2 nanoparticles are more suitable for yellow light emission owing to the high value of CCT. In the view of Khakhal et al.[15] Yb-doping in CeO_2 nanoparticles was found to improve the FM ordering that can affect the room-temperature ferromagnetic (RTFM) properties of these nanoparticles. Dilute magnetic oxides such as CeO_2 exhibit RTFM properties which are effectively influenced by the valence state, the varying percentage of dopants, and the oxygen vacancies utilized to enhance FM ordering in nanoparticles. Sundari et al.[16] showed that CeO_2, which naturally possesses diamagnetic properties, may acquire ferromagnetic properties by adding Fe. Sm-doped CeO_2 nanoparticles exhibit stronger antibacterial action against harmful bacteria, according to Balamurugan et al.[17] An extensive literature has been published on the modification of the physical and chemical properties of CeO_2 nanoparticles doped with Ag in order to demonstrate their applications in various technological possibilities.[18] As reported by Choudhary et al.[19] with the rate of electron–hole pair recombination declining, the addition of ceria to metal ions such as Fe^{3+}, Cu^{2+}, Mn^{2+}, and Ag^+ considerably improved the photocatalytic activity. According to Rao et al.[20] adding Ag improves the catalytic activity of CeO_2. According to Elango et al.[21] who found that Ag-doped CeO_2 nanocomposites had a moderate amount of antibacterial activity against harmful bacteria, these materials could be employed as an antimicrobial agent in biomedical applications. According to de Lima et al.[22] CeO_2 improves the reducibility of this oxide when combined with Ag, resulting in a larger selectivity for acetone and a lower selectivity for ethylene. Additionally, Ma et al.[23] revealed that the creation of visible light-reactive photocatalysts using Ag-modified CeO_2 is an appealing method due to its enhanced visible light absorption capability. Mittal et al. emphasized the significance of oxygen

vacancies for fast catalysis in Ag-/Au-doped CeO_2 nanoparticles.[24] Overall, doping elements like Ag favor an improvement in the visible light response of CeO_2 nanoparticles.

The main characteristics of the silver–ceria interaction are related to oxygen species over Ag particles, the morphology and size effects of both Ag and CeO_2 particles, the chemical and charge state of silver, charge transfer between silver and ceria, the type and concentrations of oxygen vacancies in the ceria structure, and the redox properties that are caused by the interaction between the Ag^+ and Ce^{3+}/Ce^{4+} pair.[25]

In this manuscript, CeO_2 has been doped with varying concentrations of Ag (*x* = 0.03, 0.05, and 0.07) using the coprecipitation route of synthesis. Because of the low cost of the starting materials, the ease of the synthesis process, and the accessibility of the equipment, the coprecipitation method is one of the most promising approaches. Also, as this method does not require high pressure or temperature, and impure ingredients are removed via filtration and washing, it is an appropriate chemical process for the preparation of nanoparticles.

To investigate the correlation between the rare-earth dopants, their concentration, and oxygen vacancy defects, we looked into the structural characteristics, dopant distribution, and correlation of Ag-doped CeO_2 NPs with oxygen vacancies. The structural characterization of the synthesized samples using XRD provides information about the phase purity and crystalline structure of the samples. The optical absorption spectra, as obtained using UV–Vis–NIR spectroscopy, has been used to find out the optical band gap. Photoluminescence spectra have been studied to explore the various electronic transitions taking place in the material using a Perkin Elmer FL 8500 system with an excitation wavelength of 325 nm. Further, to find out the presence of illuminating color in the luminescent material, the CIE (International Commission on Illumination) diagram has been plotted. These findings provide a physical explanation for the experimentally observed improved photoluminescence of Ag-doped CeO_2 nanoparticles, which can be helpful in the development of a new doped CeO_2 for optoelectronic devices.

Experimental

Synthesis of Undoped CeO_2 and $Ce_{1-x}Ag_xO_2$ Nanoparticles

The undoped CeO_2 and $Ce_{1-x}Ag_xO_2$ (*x* = 0.03, 0.05, and 0.07) samples were synthesized using the coprecipitation method given elsewhere.[12] The proper stoichiometric ratio of $CeCl_3.7H_2O$ and $AgNO_3$ with purities of 99.50% and 99.99%, respectively (Alpha Aesar) was used to synthesize $Ce_{1-x}Ag_xO_2$ nanoparticles using an NH_4OH solution

as a reducing agent. The NH$_4$OH solution was added to the precursor solution drop by drop until the pH of the final product reached 11. A light-yellow precipitate was produced after stirring the solution for around 4 h while maintaining the temperature at 50 °C. The precipitate was then dried at room temperature after being rinsed with ethanol and distilled water. The additional precipitate was annealed in a vacuum furnace for 6 h at 700°C to produce a powder that contained both undoped CeO$_2$ and nanoparticles with 3%, 5%, and 7% Ag doping. The preparation of the desired nanoparticles is effectively explained by the chemical reaction pathway detailed here.

Characterization of Nanoparticles

The crystalline structure of the synthesized samples was investigated using a Bruker D8 Advance diffractometer (XRD). X-rays were produced using Cu (=1.5406 Å) radiation. Diffraction patterns were recorded at a scanning speed and counting rate of 0.020 min^{-1} and 5 s per step, respectively, in the 2θ range between 200 and 800. A Shimadzu UV-3600 Plus spectrophotometer was used to analyze the UV–Vis absorbance spectra. The wavelength range was taken as 200–800 nm, with BaSO$_4$ as a standard sample. Using a Perkin Elmer FL 8500 system with an excitation wavelength of 325 nm, the photoluminescence spectra were measured with a wavelength range of 380–540 nm for the undoped CeO$_2$ and Ag-doped CeO$_2$ nanoparticles.

Results and Discussion

Local Geometrical Structure

Figure 1 represents the XRD patterns of undoped CeO$_2$ and Ce$_{1-x}$Ag$_x$O$_2$ (x = 0.03, 0.05, and 0.07) nanoparticles. The undoped CeO$_2$ sample represents well-defined peaks at 2θ values corresponding to the (1 1 1), (2 0 0), (2 2 0), (3 1 1), (2 2 2), (4 0 0), (3 3 1), and (4 2 0) planes. All these diffraction peaks may be attributed to the CeO$_2$ fluorite face-centered cubic (fcc) structure with the space group Fm3m (JCPDS No.004-0593). No other peaks relevant to the impurities were detected in the XRD patterns of undoped CeO$_2$ and Ag-doped samples at lower concentrations (x = 0.03), indicating the good crystalline purity of synthesized nanoparticles. As shown in Fig. 1, at higher Ag doping (x = 0.05, 0.07), two additional peaks corresponding to the (1 1 1) and (2 1 1) planes of the hexagonal phase of Ag$_2$O (JCPDS No. 72-2108) appeared in the XRD pattern of the Ag-doped CeO$_2$ nanoparticles. The presence of additional peaks indicates the formation of crystalline Ag$_2$O particles on the surface of the CeO$_2$ lattice.[26] In addition to their incorporation into the host lattice, the impurity peaks correspond to the inappropriate substitution of Ag$^+$ cations, limiting the ability to control the Ag doping concentration after the optimum value (x = 0.03). The XRD analysis revealed that the intensity of the diffraction peaks shows variation with the incorporation of Ag$^+$

Fig. 1 The XRD patterns of undoped CeO$_2$ and Ce$_{1-x}$Ag$_x$O$_2$ (x = 0.03, 0.05 and 0.07) nanoparticles; *inset* the shifting of the (111) and (200) planes towards the lower angle side.
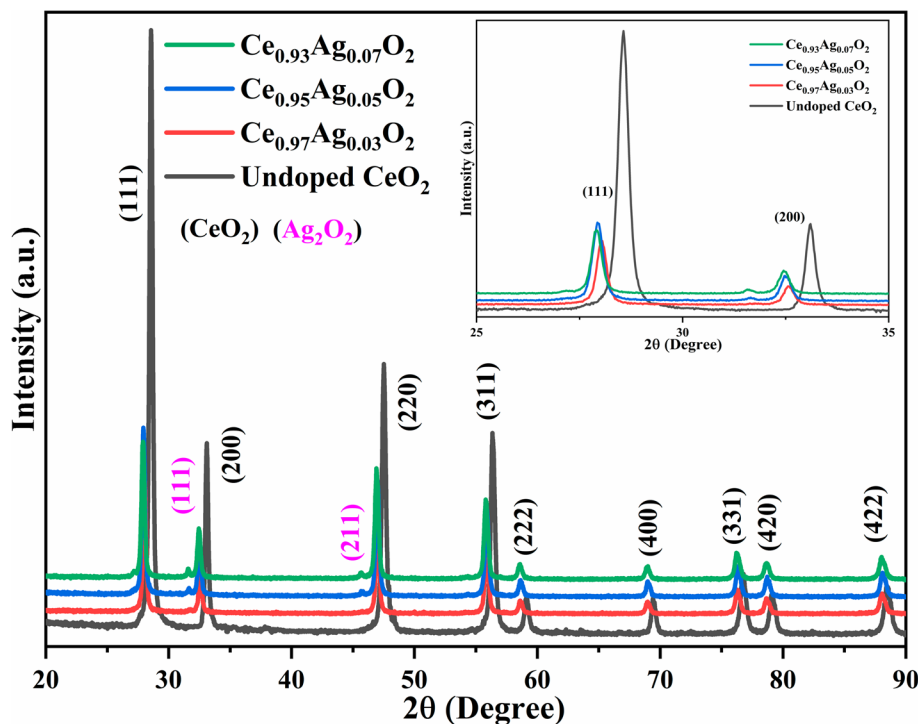
cations. A higher intensity value indicates that the crystallinity is improving, whereas a lower intensity value indicates that the samples have low crystallinity. In addition, the position of the prominent peak (1 1 1) corresponding to CeO$_2$ (listed in Table I) exhibits a shift towards the lower angle side with an increase in Ag content. The decrease in the 2θ value with an increase in d spacing can be explained on the basis of the Bragg diffraction law. The results are further confirmed by calculating the lattice parameters, which include the lattice constant (a). The crystalline size (D) can be measured using Scherrer's equation[27]:

$$D = \frac{K\lambda}{\beta \cos\theta} \tag{1}$$

where all the parameters have their usual meaning. The lattice spacing and lattice parameter corresponding to (111) plane and the corresponding results are set out in Table I.

As shown in the inset of Fig. 1, the shifting of the 2θ value towards the lower angle side is attributed to an increase in the lattice constant due to the replacement of the small Ce^{4+} ion (ionic radius = 0.097 nm) by larger Ag$^+$ ion (ionic radius = 0.126 nm), and the creation of another cation Ce^{3+} (0.114 nm) into the crystal lattice site.[28] In addition, a substantial number of oxygen vacancies are produced due to discrepancies in the ionic radii of the Ag$^+$ and Ce^{3+} ions to compensate for charge neutrality.[29] It is to be expected that incorporation of the Ag$^+$ ion in CeO$_2$ acquires a high amount of energy.[30] The crystallite size gradually increases as the Ag$^+$ cation ($x = 3\%$) is doped in the CeO$_2$ lattice, which could result from reformation and the growth of primary Ag-CeO$_2$ particles that are formed due to interactions between Ag-Ce precursors during coprecipitation.[31] The crystal imperfections and distortions can also induce strain in the nanoparticles. Generally, the peaks shift towards the side with the lower angle due to lattice expansion and strain formation, whereas the sharpness of the peak represents the good crystalline nature of the sample.[32]

Table I indicates that the values of d and a are increasing with an increase in Ag$^+$ concentration. The values of strain provided in Table I are tensile strain (also termed microstrain). The promotion of the formation of oxygen vacancies through tensile strain over compressive strain has been addressed by Dongwei et al.[33] Tensile strain results in a reduced overlap between the O 2p and Ce 5d orbitals as well as the 4f orbitals, which weakens the Ce-O bond. This decrease in the O 2p orbital bandwidth correlates to tensile strain, thus generating oxygen vacancies in the doped CeO$_2$. In contrast, in the case of compressive strain, the bandwidth of the O 2p orbital increases compared to the system with tensile strain. As a result, the larger bandwidth shows strong overlapping of O 2p and Ce orbitals, therefore strengthening the Ce-O bond.[34] These results unequivocally show that oxygen vacancy generation may be easily tuned by lattice strain. The microstrain varies according to crystallite size, i.e., a lower value of D gives a higher magnitude of strain due to the agglomeration of nanoparticles, as calculated using Scherrer's equation. As shown in Table I, microstrain occurs even in undoped CeO$_2$ because of oxygen vacancy defects and Ce^{3+} ions on the structure's surface.[35] After optimal doping of Ag ($x = 0.03$), the crystallite size was found to be reduced, while the value of lattice strain began to increase with an increase in Ag doping ($x = 0.05$, 0.07). Considering that particle size and strain both contribute to line broadening, line breadth is simply:

$$\beta_{hkl} \cos\theta = \frac{K\lambda}{D} + 4\varepsilon \sin\theta \tag{2}$$

This equation is the Williamson–Hall (W–H) equation of $\beta_{hkl} \cos\theta$ plotted against $4\sin\theta$, and the linear fit to the curve produces the strain and particle size, which can be calculated using the slope and intercept, respectively.[36]

Figure 2a represents the W–H analysis of undoped CeO$_2$ and Ce$_{1-x}$Ag$_x$O$_2$ ($x = 0.03$, 0.05, and 0.07) nanoparticles. Table I summarizes the calculated values of crystallite sizes and strains estimated from the W–H equation. The results signify the variation in the average crystallite size from 47 nm for undoped CeO$_2$ to 45 nm, 37 nm, and 40 nm for Ce$_{1-x}$Ag$_x$O$_2$ ($x = 0.03$, 0.05, and 0.07) respectively. However, a better measurement of size–strain parameters

Table I The calculates values of lattice parameter (a), lattice spacing (d), crystallite size (D), full width at half-maxima (FWHM), and microstrain (ε) of undoped and Ce$_{1-x}$Ag$_x$O$_2$ ($x = 0.0 3$, 0.05, and 0.07) using Scherrer's equation, a W–H plot, and the SSP method

Samples	Lattice spacing d (Å)	Lattice parameter a (Å)	FWHM $\times 10^{-3}$	Crystalline size D (nm)			Microstrain (ε)	
				$D = \frac{K\lambda}{\beta\cos\theta}$	W–H plot	SSP method	$\varepsilon = \frac{\beta\cos\theta}{4} \times 10^{-4}$	W–H plot $\times 10^{-4}$
Undoped CeO$_2$	1.846	5.410	4.86	26	47	34	13.30	12.4
Ce$_{0.97}$Ag$_{0.03}$O$_2$	1.861	5.457	4.13	29	45	37	11.89	9.05
Ce$_{0.95}$Ag$_{0.05}$O$_2$	1.863	5.459	4.52	28	37	33	11.92	6.17
Ce$_{0.93}$Ag$_{0.07}$O$_2$	1.865	5.465	4.34	28	40	41	11.98	7.57

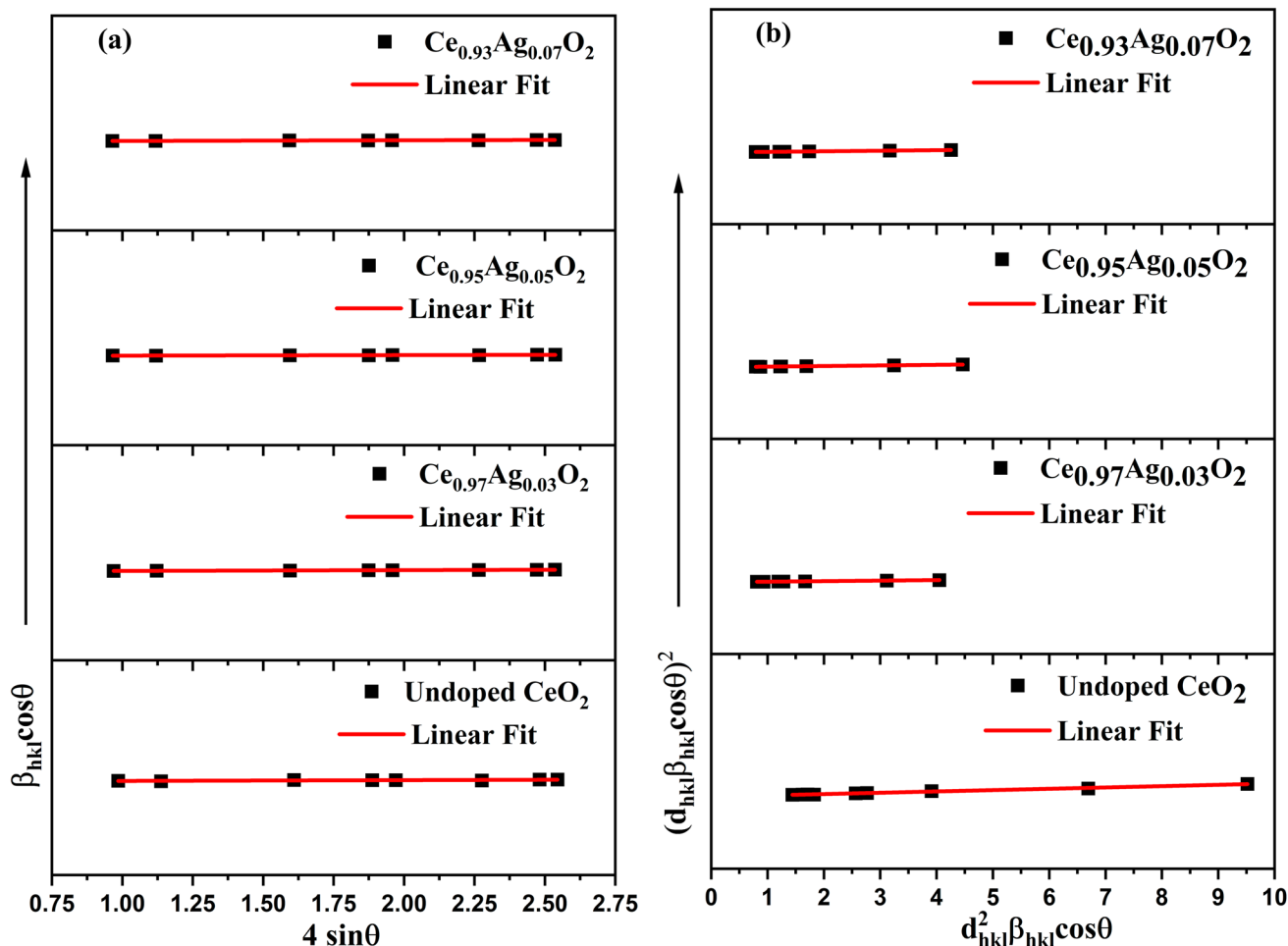**Fig. 2** (a) W–H plots of $\beta_{hkl} \cos\theta$ versus $4\sin\theta$, and (b) SSP of $\left(d_{hkl}\beta\cos\theta\right)^2$ versus $d^2\beta_{hkl}\cos\theta$ of undoped CeO₂ and Ce$_{1-x}$Ag$_x$O₂ ($x = 0.03$, 0.05, and 0.07) nanoparticles.

can be estimated by a size–strain plot (SSP), assuming that the crystallite size and strain can be described by Lorentzian and Gaussian functions, respectively. Therefore, we have:

$$\left(d_{hkl}\beta\cos\theta\right)^2 = \frac{K\left(d^2\beta_{hkl}\cos\theta\right)}{D} + \left(\frac{\varepsilon}{2}\right)^2 \tag{3}$$

In this case, crystallite size can be calculated using the slope of the linearly fitted curves, and the y-intercept yields the strain.[37] Figure 2b represents the SSP analysis of undoped CeO₂ and Ce$_{1-x}$Ag$_x$O₂ ($x = 0.0\ 3$, 0.05, and 0.07) nanoparticles. Table I indicates that variation in the broadness of the peak affects the crystallite size. The higher value of β indicates a lower value of D. The average crystallite sizes resulting from the W–H plot and the SSP method indicate a similar trend with varying numerical values with increasing Ag dopant content.

Absorption Spectroscopy

The UV–Vis spectra of undoped CeO₂ and Ce$_{1-x}$Ag$_x$O₂ ($x = 0.03$, 0.05, and 0.07) nanoparticles are shown in Fig. 3a. The absorption peaks have been recorded in the range of 200–800 nm. All the samples exhibit strong absorbance near 300 nm, with their corresponding absorption peak in the UV range. These peaks arise due to charge transfer from the $2p$ state of the valence band of O^{2-} to the 4f state of the conduction band (CB) of Ce^{4+}. As a result, the electrons in the Ce^{4+} (4f) conduction band and the holes in the O^{2-} (2p) valence band (VB) directly recombine.[38] From the absorption data, the value of the optical band gap energy (E_g) of the undoped and Ag-doped CeO₂ samples is calculated using Tauc's relationship[39]:

$$\alpha h\nu = A\left(h\nu - E_g\right)^n \tag{4}$$

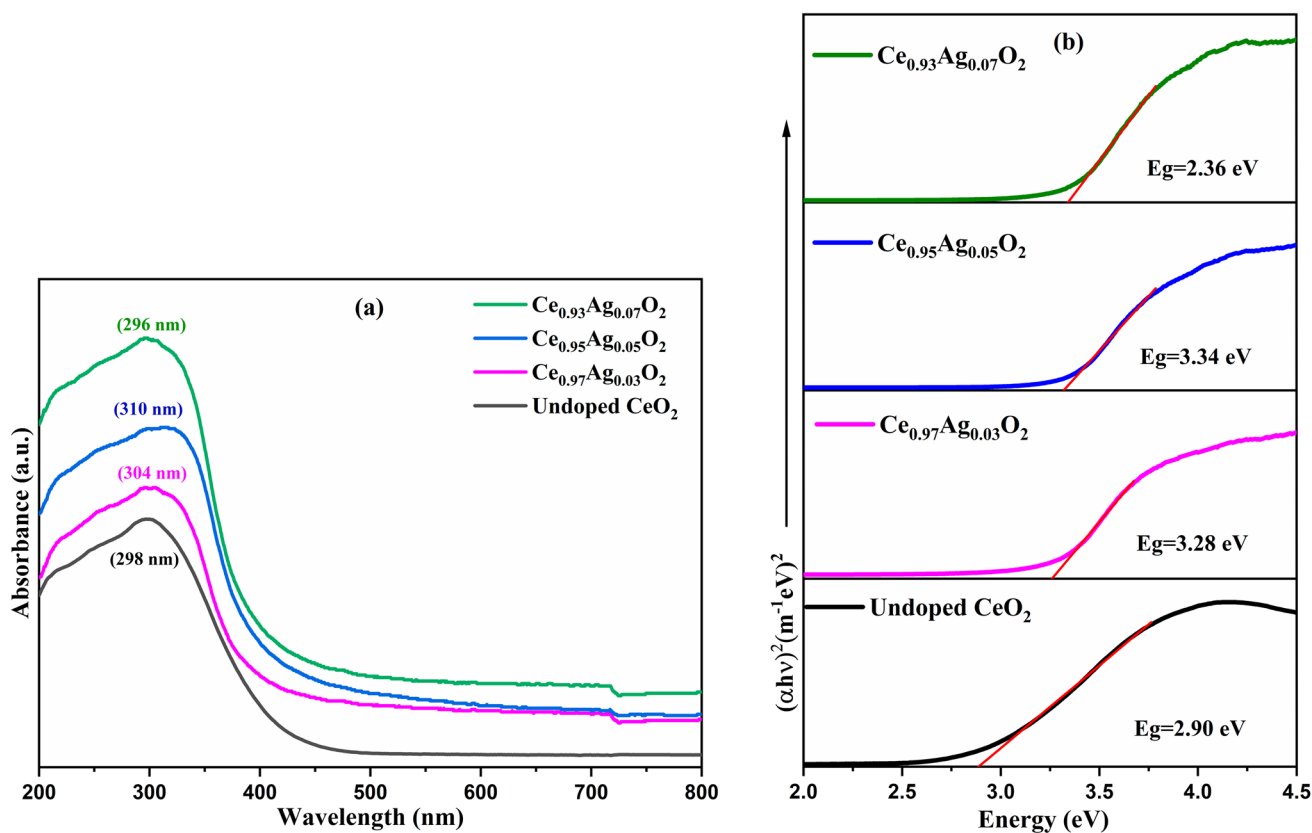**Fig. 3** (a) Room temperature optical absorption spectrum and (b) the Tauc's plot of undoped CeO_2 and $Ce_{1-x}Ag_xO_2$ ($x = 0.03, 0.05$ and 0.07) nanoparticles.

Table II The band gap energy as calculated using Tauc's relationship, the energy equation, the derivation method, and Urbach energy for the undoped and CeO_2 and $Ce_{1-x}Ag_xO_2$ ($x = 0.03, 0.05$ and 0.07)

Samples	E_g (eV)			Urbach energy (eV)	Refractive index (n)
	Tauc's relationship	Energy equation	Derivation method		
Undoped CeO_2	2.90	3.36	3.40	0.2510	2.4245
$Ce_{0.97}Ag_{0.03}O_2$	3.28	3.42	3.43	0.4283	2.3255
$Ce_{0.95}Ag_{0.05}O_2$	3.34	3.43	3.47	0.3647	2.3110
$Ce_{0.93}Ag_{0.07}O_2$	3.36	3.45	3.49	0.2731	2.3063

where all the parameters have their usual meanings. Table II incorporates the calculated value of band gap energy (E_g) for all the samples. Figure 3b depicts the graphical representation of $(\alpha h\nu)^2$ versus energy ($h\nu$) for the undoped CeO_2 and $Ce_{1-x}Ag_xO_2$ ($x = 0.03, 0.05$, and 0.07) nanoparticles. The undoped CeO_2 nanoparticles have a direct band gap energy of 2.90 eV, and the band gap value steadily increases with increasing Ag dopant concentration.

Table II shows the rise in the band gap with Ag doping as calculated using Tauc's formula, the energy equation, and the derivation method. The rise in band gap with blue shifting in the absorption spectra with Ag doping in CeO_2 nanoparticles could be explained on the basis of the change of the Ce^{4+} to Ce^{3+} state, which suggests the widening in the direct charge–transfer transition gap between the O $2p$ and Ce $4f$ bands and therefore the rise in the optical band gap. Further, the blue shift may also correspond to s decrease of Ce^{3+} concentration along with oxygen vacancies during the annealing process, which suppresses some localized defect states within the band gap, thus the deficiency in the vacancy content is therefore responsible for band gap widening.[40] Another effect that could be useful to explain the blue shift is the Burstein–Moss (BM) effect, which relies on the generation of a high charge carrier density such that the Fermi level is shifted to the CB. As a result, energy transitions near the bottom of the band are prevented, and the band gap becomes widened[41]:

$$\Delta E_g^{BM} = \frac{h^2}{2m_{vc}^*}\left(3\pi^2 n_e\right)^{\frac{2}{3}} \tag{5}$$

where m_{vc}^* and n_e are an effective mass and concentration of electrons, respectively and h is Plank's constant. The generation of a high number of free electrons above the Mott critical density partially fills the $4f$ orbital of Ce which blocks the lowest state and leads to an increase in the band gap.[42] So, it can be concluded that the Ag-doped CeO$_2$ samples are enough sufficient to cross the limit of the Mott critical density for the BM effect to occur. Thus, the BM effect and the carrier concentration are both responsible for widening the band gap. In order to confirm the formation of defects between the CB and the VB, the Urbach energy has been calculated using:

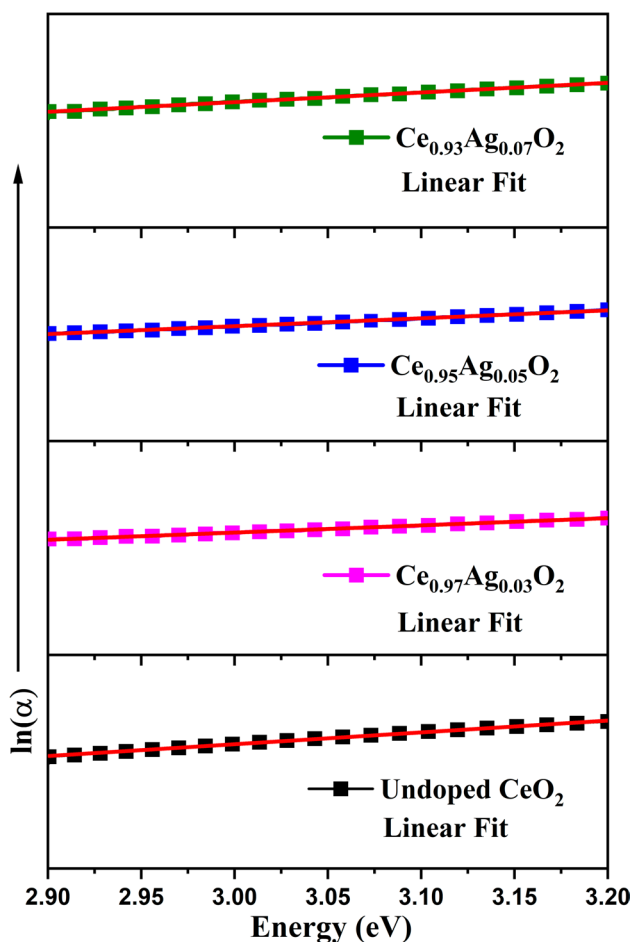$$\alpha = \alpha_0 \exp\left(\frac{h\nu}{E_u}\right) \tag{6}$$

Fig. 4 lnα versus photon energy for undoped CeO$_2$ and Ce$_{1-x}$Ag$_x$O$_2$ ($x = 0.03$, 0.05 and 0.07) nanoparticles.

Figure 4 illustrates the logarithm of the absorption coefficient plotted against the photon energy, and the Urbach energy is determined by the inverse of the slope.[43] The Urbach energy for the undoped CeO$_2$ and Ce$_{1-x}$Ag$_x$O$_2$ ($x = 0.03$, 0.05, and 0.07) is listed in Table II, and the calculation reflects that even undoped CeO$_2$ yields an Urbach energy of 0.2510 eV, indicating the presence of some defect states. After introducing Ag doping ($x = 0.03$), the rise in Urbach energy shows the generation of more defects and localized states due to the substitution of Ag cations into the CeO$_2$ lattice. Further, the decrease in the magnitude of Urbach energy with increasing Ag dopant concentration ($x = 0.05$, 0.07) attributes to a reduction in structural defects along with oxygen vacancies, and the crystallite size with higher dopant concentration, as mentioned above. Such behavior may be associated with structural changes after the addition of Ag$_2$O. These results agree well with the XRD measurements, from which we have found that the particle size increases up to an optimal Ag-doping concentration ($x = 0.03$) and after which the particle size is reduced, which suggests the inappropriate substitution of Ag$^+$ ions at higher doping concentrations.

The band gap (E_g) and Urbach energy (E_u) of nanoparticles can change their refractive index, changing their optical properties and tunability. These changes can be utilized to make use of these materials for optoelectronic devices. The refractive index for the prepared samples was calculated as per Refs. 44 and 45 and are tabulated in Table II.

In order to further confirm the generation of defects with the introduction of the Ag dopant, the relative energy positions of the CB and VB have also been investigated using the Mullikan electronegativity formula, which allows us to better understand the mechanism of electron and hole separation:

$$E_{CB}(CeO_2) = \chi(CeO_2) - E^c - \frac{E_g}{2} \tag{7}$$

$$E_{VB}(CeO_2) = E_g - E_{CB}(CeO_2) \tag{8}$$

where all the parameters are provided in Ref. 46, with $\chi = 5.56$ eV for CeO$_2$). Figure 5 represents the energy band diagram of the undoped CeO$_2$ and Ce$_{1-x}$Ag$_x$O$_2$ ($x = 0.03$, 0.05, and 0.07) nanoparticles, showing that the positions of the CB are shifted towards a high negative potential, whereas the positions for VB are shifted towards a positive potential with an increase in the doping concentration of the Ag cations. Because of their well-coupled band structure, these samples are advantageous for the separation of photogenerated charge carriers with variations in band positions.[47]

The estimated values of the CB and VB positions of undoped CeO$_2$ and Ce$_{1-x}$Ag$_x$O$_2$ ($x = 0.03$, 0.05, and 0.07) is shown in Fig. 5. The absorption spectrum indicates that

Fig. 5 Energy band diagram of undoped CeO_2 and $Ce_{1-x}Ag_xO_2$ ($x = 0.03, 0.05$ and 0.07) nanoparticles.
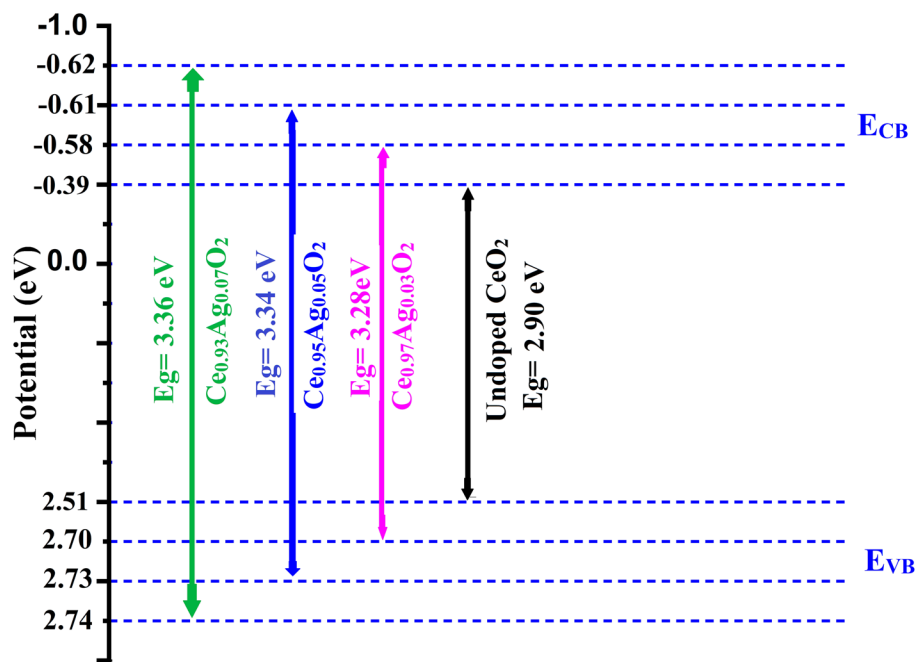
absorption maxima are blue-shifted towards lower wavelengths with increasing Ag content, corresponding to a band gap from 3.24 eV to 3.37 eV, owing to the BM effect. The results justify that the absorption peaks of Ag-doped CeO_2 nanoparticles have most probably originated due to intra-band formation. The conduction electron is responsible for the intra-band excitations from the lowest energy level to the highest energy level, as allowed by the quantum number principle.[48]

Photoluminescence Analysis

The photoluminescence (PL) spectroscopic technique is a useful tool to evaluate the electronic structure of a material. The PL results help in realizing the role of crystalline defects, which are generated due to photo-excited electron–hole pairs in semiconductors. Figure 6 represents the room-temperature PL spectra of undoped and Ag-doped CeO_2 nanoparticles recorded at the excitation wavelength of 325 nm. It has been confirmed that the emission in CeO_2 nanoparticles originates due to the transition from the Cerium 4f band to the oxygen 2p VB.[46] The UV luminescence band between 380 and 400 nm is also shown, comprising of two peaks at 385 nm and 395 nm. Exciton–exciton collisions that combine charge carriers give rise to near-band edge (NBE) luminescence at 385 and 395, which is attributed to UV emissions.[30] The UV emission band near to 400 nm is supposed to arise from indirect excitonic transitions involving (Ce^{4+} $4f^0 \rightarrow Ce^{3+}$ $4f^1$).[49] In addition, emission peaks are also observed at 419 nm, 438 nm, 450 nm, 467 nm, 481 nm, 491 nm, and 517 nm which correspond

to deep level emissions and are stronger. The formation of deep and shallow states in the CeO_2 forbidden gap can be correlated with various imperfections, such as Schottky and Frenkel defects.[50] The charge transfer shift from the oxygen vacancy defect level to the O 2p level is what causes these emission peaks to appear. The emission peaks at 419 nm, 438 nm, and 450 nm belong to the violet–blue region and occur due to radiating traps at the grain boundaries. The emission peaks around 467 nm, 481 nm, and 491 nm belongs to blue–green emissions, while the peak measured at 517 nm corresponds to a green emission.[51]

Different literature provides various causes for the generation of these emission peaks, such as Meng et al.[52] who suggested that transition from different defect levels to O 2p band could be ascribed to the wide emission band from 445 nm to 550 nm. Wang et al.[53] reported that an emission band at 467 nm could be attributed to defects like dislocation, which are responsible for fast oxidation transport. According to Kurok et al.[54] the emission band located at 481 nm is due the transition from the ionized oxygen defect level to the VB (Table III).

In the PL spectra of the Ag-doped CeO_2 samples, neither a change in the defect emission's position nor the emergence of an Ag-related emission peak have been observed. Figure 6b also depicts the rise in the PL intensity, indicating that defects are suppressed with a higher Ag dopant ($x = 0.05$, 0.07). The increased PL intensity can be attributed to the presence of a small number of non-radiative defects in the samples. Different factors are responsible for varying the intensity of the emission peaks, such as the radiative or non-radiative nature of the oxygen vacancies responsible for

decreasing or increasing the intensity peaks. As reported by Kumar et al.[55] the increasing PL intensity corresponds to a lack of oxygen vacancies. The XRD measurements reflect that doping CeO$_2$ with Ag at a lower concentration
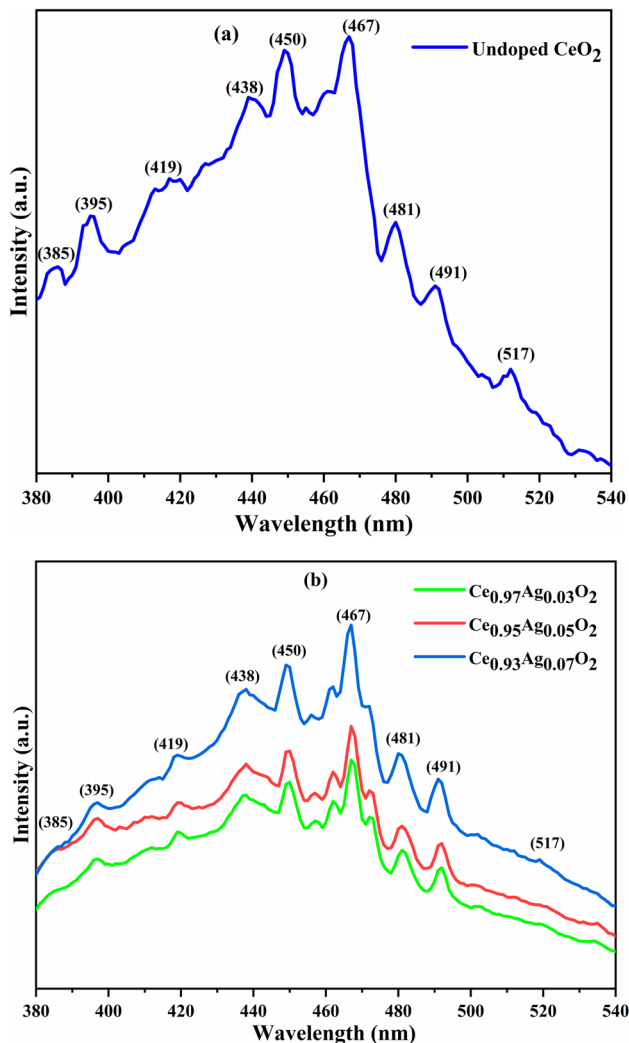

Fig. 6 The PL spectra of (a) undoped CeO$_2$ and (b) Ce$_{1-x}$Ag$_x$O$_2$ (x = 0.03, 0.05 and 0.07) nanoparticles recorded using an excitation wavelength of 325 nm at ambient temperature.

(x = 0.03) distorts the lattice and thereby produces a large number of oxygen vacancies, which trapped the excited electrons and emitted them directly as light photons. It may also be possible that the oxygen vacancies recombine with the Ce^{3+} hole by releasing the excited electrons into the dopant.[50] These trapped electrons may recombine with the holes over a longer period of time, which would reduce the luminescence intensity.[56, 57] In contrast, as we go to a higher doping concentration (x = 0.05, 0.07), the decrease in defect concentration favors a high mobility of charge carriers which in turn reduces the excitonic recombination rate. The degradation in the defects is consistent with the blue shift and the Urbach energy of Ag-doped CeO$_2$ nanoparticles.

CIE Analysis

In order to analyze the emission intensities and dominant emission wavelengths, the CIE 1931 system, also known as the International Commission on Illusion, has been used. Understanding the qualitative and quantitative examination of the PL spectrum of luminous materials and the components of their color is made easier with the aid of the CIE analysis.[58] The color produced by the luminescent material or by any light source can be understood by considering the dimensional quantities, known as "color matching functions", such as x(λ), y(λ), and z(λ).[59] The addition of three tristimulus values (X, Y, Z) gives the real spectral color, as shown elsewhere.[60] As set out in Table IV, the calculated (x, y) coordinates of the prepared sample are (0.3104, 0.3523), (0.3502, 0.3618), (0.3558, 0.3689), and (0.3643, 0.3745), corresponding to undoped CeO$_2$ and Ce$_{1-x}$Ag$_x$O$_2$ (x = 0.03, 0.05, and 0.07) nanoparticles. The visible colors along with the indexed coordinates have been revealed through the horseshoe diagram in the CIE diagram (Fig. 7), which shows that the CIE color coordinates of undoped and Ag-doped CeO$_2$ nanoparticles lie near the white point (CIE standard illuminate C) based on the NTSE system.[61,62] As the concentration of the Ag$^+$ dopant increases, the x and y coordinates also increase, indicating that the CIE coordinates are shifting a little bit compared to the undoped CeO$_2$, which still satisfies the criterion for maintaining its operation in the white

Table III Various defect emission transitions and their reasons for emission

Emission peak (nm)	Corresponding region	Reasons of emission	References
385	UV (NBE)	Recombination of charge carriers via exciton–exciton collisions involving transition Ce^{4+} 4f^0 to Ce^{3+} 4f^1	27, 43
395			
419	Visible (violet–blue)	Radiating traps at grain boundaries.	46, 48
438			
450			
467	Visible (blue–green)	Defects such as dislocation	49
481	Visible (blue–green)	Transition from ionized oxygen defect level to VB	50

Table IV The CIE diagram's parameters for color x, y, λ_d, color purity, color rendering index (*CRI*), and CCT values for undoped CeO_2 and $Ce_{1-x}Ag_xO_2$ ($x = 0.03$, 0.05 and 0.07) nanoparticles

Samples	X	Y	CCT (K)	λ_d (nm)	Color purity (%)	CRI
Undoped CeO_2	0.3104	0.3523	6460	502.9	7.0	89
$Ce_{0.97}Ag_{0.03}O_2$	0.3502	0.3618	4851	571.8	13.7	93
$Ce_{0.95}Ag_{0.05}O_2$	0.3558	0.3689	4692	572.6	17.5	94
$Ce_{0.093}Ag_{0.07}O_2$	0.3643	0.3745	4452	574.6	21.7	94
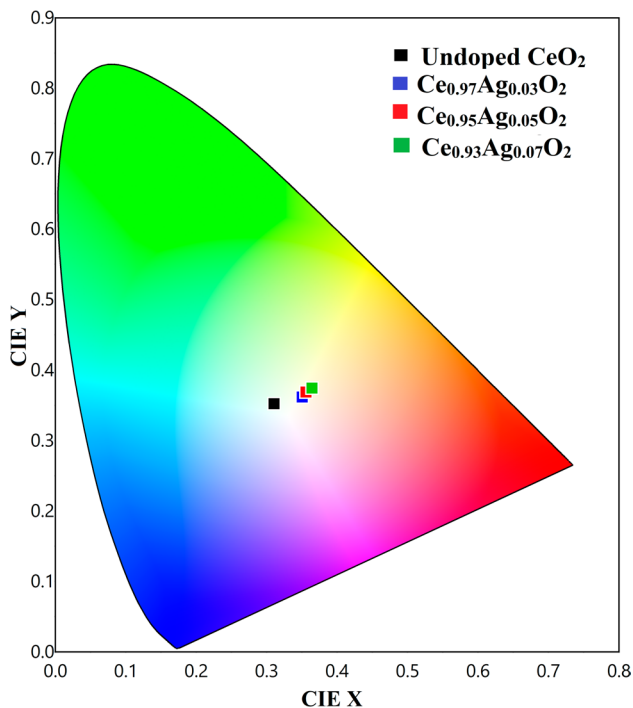
Fig. 7 The CIE chromaticity diagram of undoped CeO_2 and $Ce_{1-x}Ag_xO_2$ ($x = 0.03$, 0.05 and 0.07) nanoparticles.

region. The CCT, which measures the light source's appearance in terms of color, is another crucial factor in deciding whether to employ a material for commercial or residential lighting. If the CCT value is < 5000 K, the luminescent material can be used as a warm light source for household purposes, while a higher CCT value of > 5000 K can be used as a cool light for commercial purposes.[63] For the given set of chromaticity coordinates (x, y), the CCT values were measured using McCamy' empirical formula[64, 65:]

$$CCT = -437n^3 + 3601n^2 - 6881n + 551.43 \quad (9)$$

where $n = (x - x_e)/(y - y_e)$ with the chromaticity epicenter having the values $x_e = 0.3320$ and $y_e = 0.1858$, while x, y are the positional coordinates. The calculated values of CCT of the undoped and Ag-doped CeO_2 nanoparticles (shown in Table IV) indicate that the undoped CeO_2 exhibits a CCT value of 6460 K with CIE coordinates in the white region. Further, the CCT value begins to decrease with increasing

Ag dopant concentration, and the calculated CCT values are 4851 K, 4692 K, and 4452 K for the $Ce_{1-x}Ag_xO_2$ ($x = 0.03$, 0.05, and 0.07, respectively) nanoparticles. Ag-doped CeO_2 nanoparticles have reached CCT values of < 5000 K, making them appropriate for neutral white light sources and for outdoor site lighting, parking garages, and security lighting, where the color temperature in the range 4000–5000 K tends to be more common. Furthermore, color purity is another important factor in determining the efficacy of color emissions from luminous materials in PL spectroscopy. It measures the color saturation numerically using color coordinates and the equation given below[66]:

$$\frac{\sqrt{(x - x_i)^2 + (y - y_i)^2}}{\sqrt{(x_d - x_i)^2 + (y_d - y_i)^2}} \times 100\% \quad (10)$$

where (x, y) and (x_i, y_i) are the color coordinates of the prepared luminescent sample, and the coordinates of white light illumination (0.33, 0.33) and (x_d, y_d) are the color coordinates with the dominant wavelength. A higher value of purity indicates more saturation of color corresponding to the dominant wavelength, while a lower value of purity shows less saturation of color. The calculated color purity of undoped CeO_2 and $Ce_{1-x}Ag_xO_2$ ($x = 0.03$, 0.05, and 0.07) nanoparticles is shown in Table IV. The measurement of color purity depicts that $Ce_{1-x}Ag_xO_2$ ($x = 0.03$, 0.05, and 0.07) nanoparticles show a significant increase in the luminous color purity (13.7, 17.5, and 21.7, respectively), compared to the undoped CeO_2 nanoparticles (7.0).

The dominant wavelength is another important parameter that determines the wavelength of monochromatic spectral light which evokes an identical perception of a specific color.[35] In our case, the dominant wavelength for undoped CeO_2 and $Ce_{1-x}Ag_xO_2$ ($x = 0.03$, 0.05, and 0.07) nanoparticles is found to vary from 502 nm to 574 nm. The CRI is a measurement of the ability of the light source to predict the color of various objects in comparison to standard light sources. The CRI value of undoped CeO_2 was 89, while for $Ce_{1-x}Ag_xO_2$ ($x = 0.03$, 0.05 and 0.07) nanoparticles, the calculated values of CRI were 93, 94, and 94, respectively. However, white LEDs are most commonly used for a wide

range of applications which require a neutral white CCT at 4000 K with a higher value of CRI.[67]

Conclusions

Undoped CeO$_2$ and Ag-doped nanoparticle samples, synthesized utilizing microwave-assisted co-precipitation techniques are useful for indoor and outdoor light applications and have been characterized for structural and optical properties with varying Ag concentrations ($x = 0.03$, 0.05, and 0.07). XRD measurements reported the nanocrystalline nature with a cubic fluorite structure for all the synthesized nanoparticles with Ag$_2$O phase (having fcc geometry), and their particle size was found to increase due to tensile strain, i.e., imposed by a larger radius cation in the CeO$_2$ lattice, which were 26, 29, 28, and 28 nm, respectively. Analysis of UV–Vis–NIR absorption spectra has shown that CeO$_2$ nanoparticles exhibit variation in band gap energy with a blue shift with different Ag concentrations. The absorption spectra with increasing Ag content indicates the shifting of Fermi energy due to the incorporation of Ag cations, introducing the impurity states in the band gap region. The Urbach energy was also calculated to ascertain the existence of defects in the CeO$_2$ lattice, which seem to decline with higher Ag doping. The findings in this study have shown that Ag-doped CeO$_2$ nanoparticles are suitable for UVA absorber applications. The intensities of the PL spectra enhanced with Ag doping give rise to better excitonic states in the band structure of the Ce$_{1-x}$Ag$_x$O$_2$ nanoparticles. The higher value of CCT determined using the PL spectra shows that these nanoparticles are suitable for commercial purposes such as LEDs and outdoor site lighting. White light sources, while retaining their CIE coordinates in the white region with a high magnitude of CRI, hold potential promise for future indoor as well as outdoor lighting applications.

Conflict of interest The authors declare that they have no conflict of interest.

References

1. N.P. Gaponik, D.V. Talapin, and A.L. Rogach, A light-emitting device based on a CdTe nanocrystal/polyaniline composite. *Phys. Chem. Chem. Phys.* 1(8), 1787–1789 (1999).
2. X. Fu, D. Feng, X. Jiang, and T. Wu, The effect of correlated color temperature and illumination level of LED lighting on visual comfort during sustained attention activities. *Sustainability* 15(4), 3826 (2023).
3. C. Artini, M. Pani, M. Carnasciali, J.R. Plaisier, and G.A. Costa, Lu-, Sm-, and Gd-doped ceria: a comparative approach to their structural properties. *Inorg. Chem.* 55(20), 10567–10579 (2016).
4. Q. Yuan, H.H. Duan, L.L. Li, L.D. Sun, Y.W. Zhang, and C.H. Yan, Controlled synthesis and assembly of ceria-based nanomaterials. *J. Colloid Interface Sci.* 335(2), 151–167 (2009).
5. C. Tiseanu, V.I. Parvulescu, M. Boutonnet, B. Cojocaru, P.A. Primus, C.M. Teodorescu, C. Solans, and M.S. Dominguez, Surface versus volume effects in luminescent ceria nanocrystals synthesized by an oil-in-water microemulsion method. *Phys. Chem. Chem. Phys.* 13(38), 17135–17145 (2011).
6. P. Ji, J. Zhang, F. Chen, and M. Anpo, Orderedmesoporous CeO$_2$ synthesized by nanocasting from cubic Ia3d mesoporous MCM-48 silica: formation, characterization and photocatalytic activity. *J. Phys. Chem. C* 112(46), 17809–17813 (2008).
7. T. Alammar, H. Noei, Y. Wang, W. Grunert, A.V. Mudring, Alammar, and T. Noei, Ionic liquid-assisted sonochemical preparation of CeO$_2$ nanoparticles for CO oxidation. *ACS Sustain. Chem. Eng.* 3(1), 42–54 (2015).
8. S. Yabe, and T. Sato, Cerium oxide for sunscreen cosmetics. *J. Solid State Chem.* 171(1–2), 7–11 (2003).
9. B. Soni, S. Makkar, and S. Biswas, Effects of surface structure and defect behaviour on the magnetic, electrical, and photocatalytic properties of Gd-doped CeO$_2$ nanoparticles synthesized by a simple chemical process. *Mater Charact* 174, 110990 (2021).
10. G. Manibalan, G. Murugadoss, R. Thangamuthu, M. Rajesh Kumar, and R.M. Kumar, Facile synthesis of CeO$_2$-SnO$_2$ nanocomposite for electrochemical determination of L-cysteine. *J. Alloy. Compd.* 792, 1150–1161 (2019).
11. L. Liao, H.X. Mai, Q. Yuan, H.B. Lu, J.C. Li, C. Liu, C.H. Yan, Z.X. Shen, and T. Yu, Single CeO$_2$ nanowire gas sensor supported with Pt nanocrystals: gas sensitivity, surface bond states, and chemical mechanism. *J. Phys. Chem. C* 112(24), 9061–9065 (2008).
12. S. Soni, N. Chouhan, R.K. Meena, S. Kumar, B. Dalela, M. Mishra, and S. Dalela, Electronic structure and room temperature ferromagnetism in Gd-doped cerium oxide nanoparticles for hydrogen generation via photocatalytic water splitting. *Global Chall.* 3(5), 1800090 (2019).
13. I.Y. Habib, J. Burhan, F. Jaladi, C.M. Lim, A. Usman, N.T.R.N. Kumara, and A.H. Mahadi, Effect of Cr doping in CeO$_2$ nanostructures on photocatalysis and H$_2$O$_2$ assisted methylene blue dye degradation. *Catal. Today* 375, 506–513 (2021).
14. N.S. Leel, M. Kiran, P.A. Alvi, B. Dalela, S. Kumar, and S. Dalela, Oxygen vacancies mediated changes in ferromagnetic, optical, Photoluminescent and electronic structure properties of Ho-doped CeO$_2$ nanoparticles. *Ceram. Int.Int* 50(5), 8448–8462 (2024).
15. H.R. Khakhal, S. Kumar, D. Patidar, S. Kumar, V.S. Vats, B. Dalela, and S. Dalela, Correlation of oxygen defects, oxide-ion conductivity and dielectric relaxation to electronic structure and room temperature ferromagnetic properties of Yb^{3+} doped CeO$_2$ nanoparticles. *Mater. Sci. Eng. B* 297, 116675 (2023).
16. S.S. Sundari, S. Sugan, and G. Pabitha, Induced ferromagnetism in Fe doped CeO$_2$ nanoparticles. *Mater. Today Proc.* 5(8), 16633–16639 (2018).
17. A. Balamurugan, M. Sudha, S. Surendhiran, R. Anandarasu, S. Ravikumar, and Y.S. Khadar, Hydrothermal synthesis of samarium (Sm) doped cerium oxide (CeO$_2$) nanoparticles: characterization and antibacterial activity. *Mater. Today Proc.* 26, 3588–3594 (2020).
18. T. Ates, Synthesis and characterization of Ag-doped CeO$_2$ powders. *J. Aust. Ceram. Soc.* 57(2), 615–623 (2021).
19. S.M. Chaudhari, O.S. Gonsalves, and P.R. Nemade, Enhanced photocatalytic degradation of Diclofenac with AgI/CeO$_2$: a

20. R. Rao, F. Shao, X. Dong, H. Dong, S. Fang, H. Sun, and Q. Ling, Effect of Ag-CeO$_2$ interface formation during one-spot synthesis of Ag-CeO$_2$ composites to improve their catalytic performance for CO oxidation. *Appl. Surf. Sci.* 513, 145771 (2020).

21. M. Elango, M. Deepa, R. Subramanian, and G. Saraswathy, Investigation of structural, morphological and antimicrobial properties of polyindole/Ag doped CeO$_2$ nanocomposites. *Mater. Today Proc.* 26, 3544–3551 (2020).

22. A.F. de Lima, P.C. Zonetti, C.P. Rodrigues, and L.G. Appel, The first step of the propylene generation from renewable raw material: acetone from ethanol employing CeO$_2$ doped by Ag. *Catal. Today* 279, 252–259 (2017).

23. R. Ma, S. Zhang, T. Wen, P. Gu, L. Li, G. Zhao, and X. Wang, A critical review on visible-light-response CeO$_2$-based photocatalysts with enhanced photooxidation of organic pollutants. *Catal. Today* 335, 20–30 (2019).

24. M. Mittal, A. Gupta, and O.P. Pandey, Role of oxygen vacancies in Ag/Au doped CeO$_2$ nanoparticles for fast photocatalysis. *Sol. Energy* 165, 206–216 (2018).

25. M.E. Grabchenko, N.N. Mikheeva, G.V. Mamontov, M.A. Salaev, L.F. Liotta, and O.V. Vodyankina, Ag/CeO$_2$ composites for catalytic abatement of CO, soot and VOCs. *Catalysts* 8(7), 285 (2018).

26. A. Haghighatzadeh, Enhanced third-order optical susceptibility in Ag-doped CeO$_2$ nanostructures under pulsed Nd-YVO$_4$ laser. *Opt. Laser Technol.* 126, 106114 (2020).

27. I. Devadoss and P. Sakthivel, Effect of Mg on Cd$_{0.9-x}$Zn$_{0.1}$S nanoparticles for optoelectronic applications. *Appl. Phys. A* 126(4), 315 (2020).

28. W.M.A. El Rouby, A.A. Farghali, and A. Hamdedein, Microwave synthesis of pure and doped cerium (IV) oxide (CeO$_2$) nanoparticles for methylene blue degradation. *Water Sci. Technol.* 74(10), 2325–2336 (2016).

29. R.N. Bharathi and S. Sankar, Investigation of transport properties of Pr-doped cerium oxide nanoparticles as a solid electrolyte for IT-SOFC applications. *J. Inorg. Organomet. Polym. Mater.* 28(5), 1829–1838 (2018).

30. K. Rajesh, P. Sakthivel, A. Santhanam, and J. Venugobal, Incorporation of silver ion on structural and optical characteristics of CeO$_2$ nanoparticles: white LED applications. *Optik* 216, 164800 (2020).

31. Y. Seo, M.W. Lee, H.J. Kim, J.W. Choung, C. Jung, C.H. Kim, and K.Y. Lee, Effect of Ag doping on Pd/Ag-CeO$_2$ catalysts for CO and C$_3$H$_6$ oxidation. *J. Hazard. Mater.* 415, 125373 (2021).

32. M. Dave, S. Kumar, B. Dalela, P.A. Alvi, S.S. Sharma, D.M. Phase, and S. Dalela, Interplay of structural, optical, and magnetic properties of Ce$_{1-x}$Nd$_x$O$_{2-\delta}$ nanoparticles with electronic structure probed using X-ray absorption spectroscopy. *Vacuum* 180, 109537 (2020).

33. D. Ma, Z. Lu, Y. Tang, T. Li, Z. Tang, and Z. Yang, Effect of lattice strain on the oxygen vacancy formation and hydrogen adsorption at CeO$_2$ (111) surface. *Phys. Lett. A* 378(34), 2570–2575 (2014).

34. R.K. Hailstone, A.G. DiFrancesco, J.G. Leong, T.D. Allston, and K.J. Reed, A study of lattice expansion in CeO$_2$ nanoparticles by transmission electron microscopy. *J. Phys. Chem. C* 113(34), 15155–15159 (2009).

35. B. Choudhury and A. Choudhury, Lattice distortion and corresponding changes in optical properties of CeO$_2$ nanoparticles on Nd doping. *Curr. Appl. Phys.* 13(1), 217–223 (2013).

36. V.D. Mote, Y. Purushotham, and B.N. Dole, Williamson-Hall analysis in estimation of lattice strain in nanometer-sized ZnO particles. *J. Theor. Appl. Phys.* 6(1), 1–8 (2012).

37. A.K. Zak, W.A. Majid, M.E. Abrishami, and R. Yousefi, X-ray analysis of ZnO nanoparticles by Williamson–Hall and size–strain plot methods. *Solid State Sci.* 13(1), 251–256 (2011).

38. H.R. Khakhal, S. Kumar, S.N. Dolia, B. Dalela, V.S. Vats, S.Z. Hashmi, and S. Dalela, Oxygen vacancies and F$^+$ centre tailored room temperature ferromagnetic properties of CeO$_2$ nanoparticles with Pr doping concentrations and annealing in hydrogen environment. *J. Alloy. Compd.* 844, 156079 (2020).

39. I. Devadoss, P. Sakthivel, and S. Pauline Sheeba, Influence of Sn^{2+} ion on structural, morphological and optical characteristics of Cd$_{0.9-x}$Zn$_{0.1}$Sn$_x$S (0≤x≤ 0.06) quantum dots. *Indian J. Phys.* 95, 741–747 (2021).

40. M.Y. Chen, X.T. Zu, X. Xiang, and H.L. Zhang, Effects of ion irradiation and annealing on optical and structural properties of CeO$_2$ films on sapphire. *Physica B* 389(2), 263–268 (2007).

41. S. Soni, S. Kumar, B. Dalela, S. Kumar, P.A. Alvi, and S. Dalela, Defects and oxygen vacancies tailored structural and optical properties in CeO$_2$ nanoparticles doped with Sm^{3+} cation. *J. Alloy. Compd.* 752, 520–531 (2018).

42. I. Hamberg, C.G. Granqvist, K.F. Berggren, B.E. Sernelius, and L. Engström, Band-gap widening in heavily Sn-doped In$_2$O$_3$. *Phys. Rev. B* 30(6), 3240 (1984).

43. J. Sahu, S. Kumar, V.S. Vats, P.A. Alvi, B. Dalela, S. Kumar, and S. Dalela, Lattice defects and oxygen vacancies formulated ferromagnetic, luminescence, structural properties and band-gap tuning in Nd^{3+} substituted ZnO nanoparticles. *J. Lumin.* 243, 118673 (2022).

44. J. Arya, N.S. Leel, Aakansha, A.M. Quraishi, S.Z. Hashmi, S. Kumar, and P.A. Alvi, Enhancement of dielectric response and optical bandgap tuning with improving surface morphology of recyclable polyvinyl alcohol–CeO$_2$ polymer nanocomposites. *Phys. Status Solidi A* 221, 2300742 (2024).

45. S.B. Dangi, N.S. Leel, A.M. Quraishi, S.Z. Hashmi, S. Kumar, S. Dalela, and P.A. Alvi, Poly (vinyl alcohol)/reduced graphene oxide (rGO) polymer nanocomposites: ecological preparation and application-oriented characterizations. *Opt. Mater.* 148, 114965 (2024).

46. M.A. Khan, W. Khan, M. Ahamed, and A.N. Alhazaa, Microstructural properties and enhanced photocatalytic performance of Zn doped CeO$_2$ nanocrystals. *Sci. Rep.* 7(1), 1–11 (2017).

47. F. Donat, S. Corbel, H. Alem, S. Pontvianne, L. Balan, G. Medjahdi, and R. Schneider, ZnO nanoparticles sensitized by CuInZn$_x$S$_{2+x}$ quantum dots as highly efficient solar light driven photocatalysts. *Beilstein J. Nanotechnol.* 8(1), 1080–1093 (2017).

48. E. Saion, E. Gharibshahi, and K. Naghavi, Size-controlled and optical properties of monodispersed silver nanoparticles synthesized by the radiolytic reduction method. *Int. J. Mol. Sci.* 14(4), 7880–7896 (2013).

49. M.A. Henderson, C.L. Perkins, M.H. Engelhard, S. Thevuthasan, and C.H. Peden, Redox properties of water on the oxidized and reduced surfaces of CeO$_2$ (111). *Surf. Sci.* 526(1–2), 1–18 (2003).

50. R. Murugan, G. Vijayaprasath, T. Mahalingam, and G. Ravi, Enhancement of room temperature ferromagnetic behavior of RF sputtered Ni–CeO$_2$ thin films. *Appl. Surf. Sci.* 390, 583–590 (2016).

51. G. Jayakumar, A.A. Irudayaraj, A.D. Raj, S.J. Sundaram, and K. Kaviyarasu, Electrical and magnetic properties of nanostructured Ni doped CeO$_2$ for optoelectronic applications. *J. Phys. Chem. Solids* 160, 110369 (2022).

52. F. Meng, L. Wang, and J. Cui, Controllable synthesis and optical properties of nano-CeO$_2$ via a facile hydrothermal route. *J. Alloy. Compd.* 556, 102–108 (2013).

53. G. Wang, Q. Mu, T. Chen, and Y. Wang, Synthesis, characterization and photoluminescence of CeO$_2$ nanoparticles by a facile method at room temperature. *J. Alloy. Compd.* 493(1–2), 202–207 (2010).

54. W.M. Kwok, A.B. Djurišić, Y.H. Leung, W.K. Chan, and D.L. Phillips, Time-resolved photoluminescence from ZnO nanostructures. *Appl. Phys. Lett.* 87(22), 223111 (2005).

55. A. Kumar, S. Babu, A.S. Karakoti, A. Schulte, and S. Seal, Luminescence properties of europium-doped cerium oxide nanoparticles: role of vacancy and oxidation states. *Langmuir* 25(18), 10998–11007 (2009).

56. N. Serpone, Is the band gap of pristine TiO_2 narrowed by anion- and cation-doping of titanium dioxide in second-generation photocatalysts? *J. Phys. Chem. B* 110(48), 24287–24293 (2006).

57. P. Yang, P. Deng, and Z. Yin, Concentration quenching in Yb: YAG. *J. Lumin.* 97(1), 51–54 (2002).

58. A.K. Tangra, S. Singh, N.X. Sun, and G.S. Lotey, Investigation of structural, Raman and photoluminescence properties of novel material: $KFeO_2$ nanoparticles. *J. Alloy. Compd.* 778, 47–52 (2019).

59. R. Vijayakumar and K. Marimuthu, Luminescence studies on Ag nanoparticles embedded Eu^{3+} doped boro-phosphate glasses. *J. Alloy. Compd.* 665, 294–303 (2016).

60. J. Sahu, S. Kumar, V.S. Vats, P.A. Alvi, B. Dalela, S. Kumar, and S. Dalela, Exploring the defects and vacancies with photoluminescence and XANES studies of Gd^{3+}-substituted ZnO nanoparticles. *Part. Part. Syst. Charact.* 39(10), 2200116 (2022).

61. J.S. Kumar, K. Pavani, T. Sasikala, A.S. Rao, N.K. Giri, S.B. Rai, and L.R. Moorthy, Photoluminescence and energy transfer properties of Sm^{3+} doped CFB glasses. *Solid State Sci.* 13(8), 1548–1553 (2011).

62. A.K. Vishwakarma, K. Jha, M. Jayasimhadri, A.S. Rao, K. Jang, B. Sivaiah, and D. Haranath, Red light emitting $BaNb_2O_6$: Eu^{3+} phosphor for solid state lighting applications. *J. Alloy. Compd.* 622, 97–101 (2015).

63. R. Singh, A. King, and B.B. Nayak, Influence of dopant concentration on powder morphology and photoluminescence characteristics of red-emitting Eu^{3+}-doped ZnO. *Optik* 247, 167870 (2021).

64. D.A. Hakeem, J.W. Pi, S.W. Kim, and K. Park, New Y_2 $LuCaAl_2SiO_{12}$: Ln (Ln=Ce^{3+}, Eu^{3+}, and Tb^{3+}) phosphors for white LED applications. *Inorg. Chem. Front.* 5(6), 1336–1345 (2018).

65. K.M. Sandeep, S. Bhat, and S.M. Dharmaprakash, Structural, optical, and LED characteristics of ZnO and Al doped ZnO thin films. *J. Phys. Chem. Solids* 104, 36–44 (2017).

66. N.S. Leel, M. Kiran, M.K. Kumawat, P.A. Alvi, V.S. Vats, D. Patidar, and S. Dalela, Oxygen vacancy driven luminescence, ferromagnetic and electronic structure properties of Eu doped CeO_2 nanoparticles. *J. Lumin.* 263, 119981 (2023).

67. S. Nizamoglu, G. Zengin, and H.V. Demir, Color-converting combinations of nanocrystal emitters for warm-white light generation with high color rendering index. *Appl. Phys. Lett.* 92(3), 031102 (2008).